The Tip60/Ep400 chromatin remodeling complex impacts basic metabolic and cellular functions in cranial neural crest-derived tissue during early orofacial development

Sebastian Gehlen-Breitbach[1]*, Theresa Schmid[1,2]*, Matthias Weider[2], Michael Wegner[1#], Lina Gölz[2#]

[1]Institut für Biochemie, Emil-Fischer-Zentrum, Friedrich-Alexander-Universität Erlangen-Nürnberg, D-91054 Erlangen, Germany, [2]Zahnklinik 3 -Kieferorthopädie, Universitätsklinikum Erlangen und Friedrich-Alexander-Universität Erlangen-Nürnberg, D-91054 Erlangen, Germany

* These authors should both be considered as co-first authors.

[#] Corresponding authors

Correspondence to: Prof. Dr. Lina Gölz (lina.goelz@uk-erlangen.de)

or Prof. Dr. Michael Wegner (michael.wegner@fau.de)

Institut für Biochemie, FAU Erlangen-Nürnberg

Fahrstrasse 17, D-91054 Erlangen, Germany

phone: +49 9131 8524620; fax: +49 9131 8522484

Running title: Kat5 and Ep400 and orofacial clefts

Key words: orofacial cleft, epigenetics, chromatin remodeling, histone acetyl transferase

Further email addresses: S. G.-B. (sebastian.gehlen-breitbach@fau.de), T.S. (Theresa.Schmid@uk-erlangen.de), Ma. W. (Matthias.Weider@uk-erlangen.de)

Abstract

The cranial neural crest plays a fundamental role in orofacial development and morphogenesis. Accordingly, mutations with impact on the cranial neural crest and its development lead to orofacial malformations such as cleft lip and palate. As a pluripotent and dynamic cell population, the cranial neural crest undergoes vast transcriptional and epigenomic alterations throughout the formation of facial structures pointing to an essential role of factors regulating chromatin state or transcription levels. Using CRISPR/Cas9-guided genome editing and conditional mutagenesis in the mouse, we here show that inactivation of Kat5 and EP400 as the two essential enzymatic subunits of the Tip60/Ep400 chromatin remodeling complexes severely affects carbohydrate and amino acid metabolism in cranial neural crest cells. The resulting decrease in protein synthesis, proliferation and survival leads to a drastic reduction of cranial neural crest cells early in fetal development and a near absence of facial structures in the absence of either protein. These findings point to a decisive role of the Tip60/Ep400 chromatin remodeling complex in facial morphogenesis and lead us to conclude that the orofacial clefting observed in patients with heterozygous KAT5 missense mutations is at least in part due to early developmental disturbances in the cranial neural crest.

Introduction

Clefts of the lip and palate, jointly referred to as orofacial clefts, rank among the most prevalent human birth defects with a frequency of 1:700 [1,2]. They occur in syndromic or non-syndromic forms [2,3]. Both genetic alterations and environmental factors contribute to their emergence [1,4,5]. Considering that proper orofacial development mainly depends on the epidermal epithelium, the cranial neural crest-derived facial mesenchyme and the reciprocal interaction between both tissues, primary defects can be localized either to the epithelium or the mesenchyme and may affect any of a number of processes including precursor cell expansion, migration, differentiation, directional growth or fusion processes [6-9].

All of these processes are under tight control of a cell-specific gene regulatory network that consists of transcription factors, regulatory RNAs and chromatin modifying factors and is regulated by several signaling pathways in a tightly controlled temporospatial pattern. Among network components, chromatin modifying factors are particularly interesting, as they are both sensitive to genetic alterations and environmental factors.

A recent study identified several de novo missense mutations in the chromodomain and the acetyl-CoA binding site of the histone acetyltransferase KAT5/TIP60 (henceforth referred to as KAT5) as cause for a syndromic form of orofacial clefting [10]. The presence of other facial dysmorphisms points to a broader role of KAT5 in the neural crest-derived mesenchyme. Additionally, KAT5 has also been reported to be a quantitative trait locus and risk factor for non-syndromic forms of orofacial clefting because of the presence of single nucleotide polymorphisms in the vicinity of the gene [11].

KAT5 is a transcriptional co-activator that functions as part of the Tip60/Ep400 chromatin remodeling complex [12,13]. In this complex, KAT5 is responsible for acetylation of histones H2A and H4, whereas the Swi/Snf-type ATPase EP400 catalyzes exchange of the acetylated H2A against the H2A.Z isoform, whose preferred association with promoter regions is usually

assumed to promote transcription. As other histone acetyltransferases, KAT5 may acetylate further proteins and have additional functions outside the Tip60/Ep400 complex [14].

Given its causal link with both syndromic and non-syndromic forms of orofacial clefts, we here decided to study the molecular function of KAT5 in the cranial neural crest and the facial mesenchyme. For conclusions about the Tip60/Ep400 complex, we extended our study to EP400, the other central subunit of the complex.

Results

To study the role of Kat5 in cells of the cranial neural crest, we first resorted to mouse O9-1 cells as a suitable and fairly well characterized cellular model [15]. In these cells, we used CRISPR/Cas9-dependent genome editing to inactivate the *Kat5* gene by targeting position 669 of the coding sequence in exon 8 (Fig. 1a). Position 669 is localized in the first common exon of *Kat5* immediately in front of the sequences coding for the MYST type HAT domain (Supl. Fig. 1a). According to Inference of CRISPR Edits (ICE) analysis, we succeeded in obtaining three independent clones that carried insertions or deletions in all four *Kat5* alleles of the tetraploid O9-1 cells (Suppl. Fig. 1b). These are predicted to lead to frameshifts and immediately ensuing premature translational termination (Suppl. Fig. 1b). Quantitative RT-PCR confirmed a drastic reduction of Kat5 transcripts in all clones (Fig. 1b). In agreement, Kat5 protein was not detectable in whole cell extracts of all three clones by Western blotting, neither as full length or truncated version (Fig. 1c).

Using total RNA from the Kat5-deficient clones and O9-1 controls, we performed RNA-seq studies. Kat5-deficient clones and controls clustered separately in PCA plots (Suppl. Fig. 1c). In total, we obtained 230 significantly deregulated genes (DEGs), of which 37 were upregulated and 193 were downregulated (absolute value of log2-fold ≥ 1, p-value ≤ 0.05) in the Kat5 knockout (ko) clones (Fig. 1d). Heatmaps of the 30 most strongly deregulated genes confirmed concordance among the samples in the respective groups (Fig. 1e). The proportion of up- versus downregulated genes is in accordance with the proposed role of Kat5 as a general activator. Gene set enrichment analysis (GSEA) revealed that DEGs were associated primarily with various aspects of the intermediate metabolism (e.g. small molecule biosynthesis/catabolism, organic hydroxyl compound, monocarboxylic acid and lipid metabolism), protein biosynthesis (e.g. ribosome biogenesis, RNA splicing, RNA nuclear export) and cellular proliferation (e.g. cell cycle, DNA replication, mitosis) (Fig. 1f). KEGG clustering of downregulated genes by

process confirmed the strong alterations in gene sets associated to carbohydrate, lipid and amino acid metabolism and revealed links to several signaling pathways (Suppl. Fig. 1d).

To see how characteristic these alterations are for the Tip60/Ep400 complex in O9-1 cells, we next performed CRISPR/Cas9 dependent genome editing for the *Ep400* gene by targeting position 3201 of the coding sequence in exon 15 (Fig. 2a). Position 3201 is localized at the ATP binding site in the front part of the split ATPase domain of Ep400 (Suppl. Fig. 2a). We obtained one clone with insertions or deletions in all four *Ep400* alleles that led to frameshifts and premature translation termination (clone 1 in Suppl. Fig. 2b). A second clone contained a frameshift mutation in three alleles and a deletion of four amino acids in the remaining allele (clone 3 in Suppl. Fig. 2b). The third had a frameshift in one allele and a six amino acid deletion in the other three (clone 2 in Suppl. Fig. 2b). Amino acid deletions were all localized in the ATP binding site and should minimally lead to inactivation of Ep400. Quantitative RT-PCR again pointed to a drastic reduction of *Ep400* transcripts in all three clones (Fig. 2b). Additionally, immunocytochemical stainings failed to detect Ep400 in all three clones arguing for an absence of the protein in all clones (Fig. 2c). Clustering of samples was again evident from the PCA plot (Suppl. Fig. 2c). In case of Ep400, we obtained a total number of 733 DEGs, 492 of them up- and 281 downregulated (absolute value of log2-fold ≥1, p-value ≤0.05) in the knockout clones (Fig. 2d). Heatmaps of the 30 most strongly deregulated genes again confirmed concordance among the samples in the respective groups (Fig. 2e). A comparable number of up- and downregulated genes has been observed in RNA-seq analyses of other Ep400-containing and Ep400-deficient samples [16-18].

Inactivation of the chromatin remodeling subunit of the Tip60/Ep400 complex predictably led to deregulation of genes associated with chromatin/chromosome organization in GSE analyses (Fig. 2f). Additionally, and similar to results on Kat5 ko clones, DEGs in Ep400 ko clones were associated with small molecule metabolism (in particular amino acid metabolism) and aspects of protein biosynthesis (e.g. translation initiation, cotranslational ER targeting of proteins,

peptide biosynthesis) according to GSEA. KEGG clustering by process confirmed that downregulation of gene expression in the absence of Ep400 affected amino acid metabolism and protein biosynthesis (via aminoacyl-tRNA biosynthesis) and again pointed to alterations in carbohydrate metabolism (glycolysis/gluconeogenesis) (Suppl. Fig. 2d). A third of the DEGs obtained for Kat5 were shared with Ep400.

KEGG pathway analysis argued that the common deregulated genes for Kat5 and Ep400 were involved in aspects of amino acid and carbohydrate metabolism as well as pluripotency (Fig. 3a). To evaluate the consequences of the observed expression changes in Kat5 ko and Ep400 ko clones, we analyzed several physiological parameters and compared them to the original O9-1 line. As a first step, we looked into the rate of ATP generation using the Seahorse XFe analyzer. In line with the RNA-seq data and the inferred changes in gene expression, we measured lower ATP generation rates by glycolysis in the absence of Kat5 or Ep400 (Fig. 3b). This was consistent between all three clones with reductions ranging from 36% - 44% among Kat5 ko clones and from 34% - 56% among Ep400 ko clones (Suppl. Fig. 3a,b). In contrast, mitochondrial ATP generation by oxidative phosphorylation was not statistically different between Kat5 and Ep400 clones on the one and controls on the other side when averaged over all three clones (Suppl. Fig. 3c). At single clone level, one Kat5 clone and two Ep400 clones exhibited statistically significant reductions in mitochondrial ATP generation (Suppl. Fig. 3d,e). However, the respective levels of reduction were mild.

To measure protein synthesis, incorporation of the puromycin analog OPP was used as a proxy for the rate of translation. Pretreatment of cells with the protein synthesis inhibitor cycloheximide was used to determine background levels (Fig. 3c, red dotted line) and analysis of control O9-1 cells defined the standard level of 100%. Intriguingly, both Kat5- and Ep400-deficient cells exhibited lower protein synthesis with 74 ± 4.8% of control levels averaged over all Kat5 ko clones and 71 ± 3.2% for Ep400 ko clones (Fig. 3c). All Kat5 ko clones and Ep400 ko clones consistently exhibited significantly decreased rates of translation (Suppl. Fig. 3f,g).

Despite the decreased rate of protein synthesis, cell death was comparable between Kat5 ko and Ep400 ko clones on the one side and control O9-1 cells on the other both when averaged over all three clones (Fig. 3d) or analyzed in each single Kat5 ko and Ep400 ko clone (Suppl. Fig. 3h,i). However, proliferation was significantly lower in the absence of Kat5 or Ep400 when determined over a period of 48h by crystal violet staining (Fig. 3e). Again, effects were consistent between ko clones with a 32-38% decrease for Kat5 ko clones and a 43-52% decrease for Ep400 ko clones (Suppl. Fig. 4a-c). This translated into a strongly reduced percentage of mitotic figures in cultures of Kat5- or Ep400-deficient O9-1 cells (Fig. 3f,g) with little variation among the ko clones for each gene (varying between 3.0% and 3.2% for Kat5 ko clones and between 2.4% and 3.7% for Ep400 clones as compared to 7.9% for the control O9-1 cells; Suppl. Fig. 4d,e). Qualitatively similar decreases were also detected in phosphohistone H3 stainings (Fig. 3h,i and Suppl. Fig. 4f,g). In summary, these results confirm that the changes in gene expression upon Kat5 or Ep400 deletion indeed result in decreased glycolysis and glycolytic ATP production, lowered protein biosynthesis and substantially reduced proliferation without detectable increases in cell death in vitro.

In the second set of experiments, we studied whether the Kat5- and Ep400-dependent changes are also relevant in cranial neural crest cells in vivo as they migrate into and form the mesenchyme of the first two pharyngeal arches that later give rise to most of the facial structures [8,19]. For this purpose, we crossed mice carrying a floxed *Kat5* or *Ep400* allele with the *Wnt1::Cre* transgene and a *Rosa26-stopflox-YFP* reporter to be able to target and identify neural-crest derived cells in the pharyngeal arches (Fig. 4a). Controls contained only the combination of *Wnt1::Cre* transgene and a *Rosa26-stopflox-YFP* reporter. Inspection of the whole mount embryos by epi- or autofluorescence revealed no major alterations or malformations at embryonic day (E) 9.5. This concerned the overall appearance, shape or size of the pharyngeal arches and the contribution of YFP-positive cranial neural crest cells in

embryos lacking one or both copies of the *Kat5* (Kat5$^{\Delta/+}$ and Kat5$^{\Delta/\Delta}$) or *Ep400* (Ep400$^{\Delta/+}$ and Ep400$^{\Delta/\Delta}$) gene (Fig. 4b).

By E10.5, a reduced presence of neural crest cells in and contribution to the first two pharyngeal arches in Kat5$^{\Delta/\Delta}$ and Ep400$^{\Delta/\Delta}$ embryos was evident from the smaller size and altered morphology of the pharyngeal arches in whole mounts and the dramatically reduced YFP autofluorescence (Fig. 4c). In heterozygously deleted, i.e. Kat5$^{\Delta/+}$ and Ep400$^{\Delta/+}$ embryos, size and autofluorescent signal of pharyngeal arches remained relatively normal at E10.5.

The cranial neural crest defect translated into a near absence of facial structures in embryos with homozygous *Kat5* deletion shortly before birth at E18.5 (Fig. 4d). Similar gross phenotypic facial malformations were also observed in embryos with homozygous *Ep400* deletion at E18.5, whereas neither mice with heterozygous *Kat5* deletion nor mice with heterozygous *Ep400* deletion exhibited any obvious facial malformations or orofacial clefts (data not shown).

In line with the reduced number of cranial neural crest cells in the pharyngeal arches of early Kat5$^{\Delta/\Delta}$ and Ep400$^{\Delta/\Delta}$ embryos, proliferation rates were substantially reduced in embryos with homozygous neural crest-specific deletion of *Kat5* or *Ep400* as determined by immunohistochemical staining for phosphohistone H3 (Fig. 5a,b; for representative stainings see Suppl. Fig. 5a,b). Intriguingly, a reduction in phosphohistone H3-positive cells was already visible at E9.5 when overall appearance of the pharyngeal arches in Kat5$^{\Delta/\Delta}$ and Ep400$^{\Delta/\Delta}$ embryos was still fairly normal (Fig. 5a; for representative stainings see Suppl. Fig. 5a). It is also noteworthy that at E9.5, phosphohistone H3-positive cells were also reduced in Kat5$^{\Delta/+}$ and Ep400$^{\Delta/+}$ embryos, whereas this effect had disappeared at E10.5 (Fig. 5a,b; for representative stainings see Suppl. Fig. 5a,b). This argues that heterozygocity of Kat5 or Ep400 may transiently decrease neural crest proliferation before cells adjust and return to normal levels. The reduced proliferation rates in Kat5$^{\Delta/\Delta}$ and Ep400$^{\Delta/\Delta}$ embryos at E10.5 were also

confirmed in BrdU incorporation studies. One hour after treatment, only 7-18% of neural crest cells had incorporated BrdU as compared to 44% in controls (Fig. 5c; Suppl. Fig. 5c).

In contrast to O9-1 cells in vitro, neural crest cells with homozygously deleted *Kat5* or *Ep400* copies additionally exhibited increased rates of apoptosis as determined by immunohistochemical stainings for cleaved caspase 3 at both E9.5 and E10.5 (Fig. 5d,e; Suppl. Fig. 6a,b). Heterozygous deletion in Kat5$^{\Delta/+}$ and Ep400$^{\Delta/+}$ embryos did not affect cell death rates in a statistically significant manner. As a consequence of reduced proliferation and increased apoptosis, neural crest cell numbers were significantly decreased in the pharyngeal arches of Kat5$^{\Delta/\Delta}$ and Ep400$^{\Delta/\Delta}$ embryos at E10.5 (shown for the second pharyngeal arch in Fig. 5f,g). In Kat5$^{\Delta/+}$ and Ep400$^{\Delta/+}$ embryos, neural crest cell numbers were normal in the pharyngeal arches at E10.5.

Discussion

In this manuscript, we have shown the relevance of Kat5 and Ep400 as the two central components of the Tip60/Ep400 chromatin remodeling complex during early development of the neural crest-derived facial mesenchyme in vitro using the O9-1 neural crest-like cell line and in vivo using conditional mouse models. In particular, we have shown that both proteins have a strong impact on the cell's metabolism, especially on carbohydrate usage and amino acids availability.

The influence of Kat5 and Ep400 on metabolic processes was detected in RNA-Seq studies on genome edited O9-1 cells lacking either Kat5 or Ep400. The magnitude of deregulated genes and the ratio of upregulated versus downregulated genes were roughly comparable with other studies on the two factors in different cellular systems [16-18,20]. There was furthermore a substantial overlap in DEGs between the RNA-seq results for the two factors. Bioinformatic analyses furthermore point to the fact that both Kat5 and Ep400 influence the same cellular processes and are thus functionally linked in O9-1 neural crest cells. Such a functional linkage is also supported by the very similar behavior of Kat5- and Ep400-deficient cells in our validation experiments.

In line with the alterations in carbohydrate and amino acids metabolism, glycolytic ATP generation and protein biosynthesis are strongly impaired. This almost certainly contributes to the substantially decreased proliferation rate of Kat5- or Ep400-deficient cells. Proliferation has been reported to be reduced after deletion of Kat5 or Ep400 in some cell types (e.g. fibroblasts), to be increased in others (e.g. cardiomyocytes) or remained unaltered (e.g. Schwann cells, oligodendroglia) [17,21-24]. This argues that the impact of the Tip60/Ep400 complex on proliferation is highly cell type-specific.

Additionally, we detected a substantially higher cell death rate in cranial neural crest cells in vivo, but not in vitro. We assume that the cells are better able to cope with metabolic

impediments in tissue culture because of the excess of nutrients provided in the medium and the possibility to switch to higher mitochondrial ATP generation. In vivo, however, migrating neural crest cells constitutively rely for energy production on aerobic glycolysis [25]. Without the ability to compensate for the energy shortage, cells may be more susceptible to cell death. As a result of the decreased proliferation and increased cell death, cranial neural crest cells fail to form sufficient amounts of mesenchyme in the pharyngeal arches that later constitute the facial mesenchyme and are required for proper formation of primary and secondary palate and final fusion processes. The resulting facial malformations and orofacial clefting in mice with homozygous neural crest-specific deletion of Kat5 or Ep400 around the time of birth are an impressive confirmation of the essential role of both gene products in facial development, including palatogenesis.

Therefore it is reasonable to assume that the early defects in the survival and expansion of the cranial neural crest are also at least in part causative for the syndromic orofacial clefts observed in patients with heterozygous Kat5 mutations and may also explain the role of Kat5 as a quantitative trait locus in non-syndromic forms [10,11].

Despite the fact that we see transient alterations in the proliferation of cranial neural crest cells in mice with heterozygous cell-specific deletion of *Kat5* and *Ep400*, we fail to observe a substantial loss of cranial neural crest cells or the occurrence of orofacial clefts. The most parsimonious explanation for the different impact of heterozygocity in humans and mice are quantitative or qualitative species-specific differences in facial development. Already due to size differences, many more neural crest cells will be needed in humans than in mice for generating sufficient amounts of facial mesenchyme. Alternatively, it cannot be excluded that there is an additional function of Kat5 and Ep400 on epidermal development that needs to be impaired for phenotypic alterations to become visible.

Conclusion

Our data show that Kat5 and Ep400 as two components of the Tip60/Ep400 chromatin remodeling complex play an important role in the metabolic reprogramming of neural crest cells and influence survival and proliferation. As a consequence, *Kat5* and *Ep400* mutations impair development of the neural crest-derived facial mesenchyme and thereby cause orofacial clefting. As the activities of Kat5 and Ep400 are themselves impacted by key metabolites such as acetyl-CoA and ATP, they may play a central role in sensing the metabolic status and metabolically reprogramming the cells by alterations in chromatin changes. This needs to be investigated in future studies, but may eventually be instrumental in manipulating the cranial neural crest in a therapeutically relevant manner.

Materials & Methods

Cell Culture

The murine neural crest cell line O9-1 was obtained from Sigma Aldrich and cultured as published [26]. Briefly, O9-1 cells were maintained on Matrigel-coated dishes in preconditioned O9-1 medium. O9-1 medium consisted of DMEM (Gibco) supplemented with 15% FCS, 0.1 mM nonessential amino acids, 0.55 µM β-mercaptoethanol, 100 U/ml penicillin and 100 U/ml streptomycin. For preconditioning, O9-1 medium was incubated with mitomycin C (Adooq Bioscience) inactivated STO mouse fibroblasts (ATCC) for 24h, sterile-filtered (Steritop, 0.22µm) and supplemented with 1000 units/ml LIF, and 25 ng/ml FGF2. The O9-1 cells were passaged every three days and reseeded at a density of 1:40.

Generation of CRISPR Knockout Lines

Kat5 and *Ep400* deficient O9-1 cell lines were obtained by CRISPR/Cas9 mediated genome editing. Guide sequences (see Fig. 1a, Fig. 2a) were determined using the CRISPOR online server (Version 4.99) [27], shortened to 19 bp length and flanked with BbsI overhangs. Corresponding oligonucleotides were inserted into BbsI-digested pX330-U6-Chimeric_BB-CBh-hSpCas9 (obtained from Addgene, plasmid #42230) [28] to generate pX330-Ep400-Ex15 and px330-Kat5-Ex8. These plasmids were co-transfected with pEGFP-N1 (Clontech) into O9-1 using Lipofectamine 2000 (Thermo Fisher). After 72 h, FACSorted EGFP-positive cells were individually seeded into 96-well plates, expanded to clones and checked for Ep400 or Kat5 expression by RT-PCR, immunocytochemistry and Western blotting. Additionally, genomic DNA around the targeted site was amplified by PCR (primer sequences see Suppl. Table 1) and sequenced to determine a knockout score using the Synthego ICE Analysis 2019, v3.0. Only clones with a score > 90% were selected.

Western blotting

Total protein lysates were generated from 80% confluent O9-1 cultures by lysis in PE-buffer (5M urea, 10% glycerol, 0.1% SDS, 0.01 M Tris pH 6.8) with cOmplete Mini protease inhibitor (Sigma-Aldrich) and sonication. Protein concentrations were determined using the BioRad DC assay. After denaturation, 20 µg of protein were electrophoresed per lane alongside a molecular weight marker on SDS-polyacrylamide gels before blotting onto nitrocellulose membranes. Membranes were washed and blocked in 1x PBST with 5% skim milk powder before consecutive incubation with primary antibody (see Suppl. Table 2)and horseradish peroxidase-coupled protein A (Thermo Scientific) and detection using Clarity Western ECL Substrate (BioRad).

Real Time PCR (RT-PCR)

Total RNA was extracted from O9-1 knockout clones at passage 2 after FACSorting and wildtype cells using the RNEasy micro kit according to the manufacturer's protocol (Quiagen). To verify the successful knockout of Ep400 or Kat5 in O9-1 clones, RNA was reverse-transcribed as described [29]. PCR reactions were run on a CFX96 Touch Real-Time PCR Detection System (BioRad) with the resulting cDNAs in Power SYBR Green Mastermix (Thermo Fisher) and 125 nmol primers (see Suppl. Table 1). Ct values were determined using Bio-Rad CFX manager software and used to calculate fold changes by the ΔΔCt method.

Immunocytochemistry

O9-1 cells were cultivated on Matrigel (Corning) coated and HCl treated glass coverslips before fixation in PBS containing 4% paraformaldehyde, permeabilization with 0.5% Triton X-100, blocking in 10% fetal calf serum, consecutive incubation with primary and secondary antibodies (see Suppl. Table 2), counterstaining of the nucleus with DAPI and mounting onto slides using Mowiol 4-88 (Carl Roth).

RNA Sequencing and bioinformatic analysis

RNA of 4 biologically independent O9-1 wildtype samples as well as 3 different Kat5 and Ep400 knockout clones was used for library generation, poly-A enrichment and RNA sequencing on the NovaSeq 6000 platform with a read length of 2 x 100 bp and an output of ~30 M clusters per sample (CeGaT, Tübingen). The generated sequence data were mapped onto the *Mus musculus* reference genome mm10 and normalized read counts were generated.

Bioinformatic analysis was performed using R version 4.2.1. The Bioconductor package *DESeq2* (version 1.36.0) [30] was applied for differential expression analysis with default parameters. The R package fgsea (version 1.22.0) [31] was used for gene set enrichment analysis and gene ontology analysis of up- and downregulated genes in the knockout samples compared to the wildtype samples with a false discovery rate (FDR) of less than 0.05. The requirements for deregulation were an absolute value of the logarithmic fold change of at least 1 and a group counts' mean larger than 100. ReViGo (http://revigo.irb.hr/) [32] was used to summarize and visualize the results. The R package pathfindR (version 1.6.4) [33] was applied to identify enriched Kyoto Encyclopedia of Genes and Genomes (KEGG) pathways in the set of deregulated genes.

Crystal Violet Staining

O9-1 cells were seeded in triplicates at a density of 10,000 cells/cm^2 on Matrigel coated dishes. One set of cells underwent fixation 2 h after seeding while a second identically seeded plate was incubated for 48 h at 37°C, 5% CO_2. Fixation was performed with 70% ethanol for 30 min at 4°C. After fixation, the cells were stained for 30 min at room temperature with crystal violet staining solution, prepared by diluting 0.5% crystal violet (Carl Roth) in 20% methanol, and consecutively washed 5 times with ddH_2O. Plates were dried overnight and the crystal violet was extracted with 0.1 M sodium citrate in 50% ethanol for 30 min at room temperature.

Absorbance was measured at a wavelength of 550 nm and proliferation rate were calculated dividing the absorbance after 48 h by the absorbance after 2 h of the corresponding wells.

Apoptosis Assay

Apoptosis of O9-1 cells was determined using propidium iodide (PI) (Fluka) staining followed by flow cytometric analysis [34]. Briefly, O9-1 cells were cultured to 70% confluency, detached, fixed with 70% ice cold ethanol for 2 h, washed two times with PBS and incubated with an extraction buffer consisting of PBS with 0.1 M Na_2HPO_4 and 0.05% Triton X-100 for 5 min at room temperature. After centrifugation at 400g for 5 min, cells were resuspended in PBS with 20 µg/ml PI and 0.2 mg/mL RNAse A (Macherey-Nagel) and incubated at RT for 30 min before analysis on a FACSCalibur (Beckton Dickinson). The rate of apoptosis was determined by calculating the fraction of cells with a sub-G1 DNA content using the Flowing Software 2.51 (Turku Bioscience Centre).

Seahorse ATP-Rate Assay

Metabolic profiling of O9-1 cells was performed using a Seahorse XFe Analyzer (Agilent). O9-1 cells were seeded in preconditioned medium into Seahorse XFe 96 well plates at a density of 20,000 cells/well and incubated overnight. Before the measurement, the cells were washed twice and incubated in fresh XF DMEM pH7.4 (Agilent) supplemented with 10 mM glucose (Carl Roth), 1 mM sodium pyruvate (Gibco) and 2 mM glutamic acid (Gibco) for 45 min at 37°C without CO_2. The cartridge was hydrated with XF Calibrant solution (Agilent) for 16 h, loaded with 75 µM oligomycin and 25 µM rotenone + antimycin A before measurement according to Agilent's ATP-Rate assay protocol. After the measurement, the cells were washed with PBS, treated with 70% ethanol for 30 min and stained with crystal violet. The obtained cell density values were used for data normalization. Total ATP generation as well as

mitochondrial and glycolytic contributions were determined using the Wave Desktop Application (Agilent) for the conducted assay.

Protein Synthesis Assay

Protein synthesis was determined by measuring the incorporation of O-propargyl-puromycin (OPP) into newly synthesized proteins [35] using the Click-it Plus OPP Alexa Fluor 647 Proteinsynthesis-Assay-Kit according to the manufacturer's manual (Thermo Fisher). Briefly, O9-1 cells were cultured in 96-well plates until 50% confluency and a pulse of OPP was applied for 30 min. Untreated cells served as negative control, cells pre-incubated with 50 µg/ml cycloheximide for 15 min defined baseline levels. After the incubation time, cells underwent fixation in 4% paraformaldehyde for 10 min before staining, image acquisition using a Leica DMI 6000 microscope, determination of the integral of the Alexa Fluor 647 intensity using FIJI [36] and division by the integral of the intensity of nuclear mask blue for normalization. For quantifications, three randomly chosen images per well were analyzed.

Generation of transgenic mice and immunohistochemical analysis

Mouse housing and experiments were in accordance with animal welfare laws and all relevant ethical regulations. They were approved by the responsible local committees and government bodies (Veterinäramt Stadt Erlangen, Regierung von Unterfranken). Mice carried floxed alleles for *Ep400* [22] or *Kat5* [37] in combination with a *Wnt1::Cre* transgene [38] for neural crest-specific deletion and a *Rosa26-stopflox-YFP* allele [39] for detection of the Cre-dependent recombination event. Genotyping was performed as described before [22,37-39]. Mice were on a mixed C3H x C57Bl/6J background and kept with continuous access to food and water under standard housing conditions in 12:12 h light–dark cycles. For bromodeoxyuridine (BrdU) labeling, 100 µg BrdU (Sigma, #B5002) per gram body weight were injected intraperitoneally into pregnant mice 1 h before tissue preparation. Embryos were obtained at E9.5, E10.5 and E18.5.

For immunohistochemistry, embryos were fixed in 4% paraformaldehyde for 3-4 h (E9.5 and E10.5) or 16 h (E18.5), washed with PBS, incubated for 7 days at 4 °C in PBS + 30% sucrose, embedded in tissue freezing medium (Leica) and stored at -80 °C until further use. Sections of 10 µm thickness were produced on a Leica cryotome C1900, placed on glass slides, washed, permeabilized with 0.5% Triton X-100 and incubated in blocking solution consisting of PBS with 10% fetal calf serum, 1% bovine serum albumin and 0.5% Triton X-100 for 2 h at RT. Afterwards, sections were incubated with primary antibodies in blocking buffer at 4°C for 16 h, and then with secondary antibodies in blocking buffer for 2 h at room temperature (for antibodies see Suppl. Table 2). Sections were counterstained with DAPI and mounted with Mowiol 4-88 (Carl Roth). Image acquisition was performed with Leica DMI 6000 microscope.

Statistical Analysis

Results from independent animals, experiments, or separately generated samples were treated as biological replicates. Sample size was $n \geq 3$ as common for this kind of study. Randomization was not possible. Investigators were not blinded in animal experiments. GraphPad Prism8 (GraphPad software, La Jolla, CA, USA) was used to determine whether differences in cell numbers, ratios or transcript levels were statistically significant by one-way ANOVA with Dunett's (comparison of genome-edited clones against control in cell culture) or Sidak's (comparison of conditional knockout against control embryos as well as heterozygous against homozygous) multiple comparisons test (*, $P \leq 0.05$; **, $P \leq 0.01$; ***, $P \leq 0.001$). The data met the assumptions of the chosen test. Variance between statistically compared groups was similar.

Data availability

All data are provided in the manuscript and its supplement or have been submitted to GEO under accession number GSE215109.

References

1 Mossey, P. A., Little, J., Munger, R. G., Dixon, M. J. & Shaw, W. C. Cleft lip and palate. Lancet 374, 1773-1785, doi:10.1016/S0140-6736(09)60695-4 (2009).

2 Leslie, E. J. & Marazita, M. L. Genetics of cleft lip and cleft palate. Am J Med Genet C Semin Med Genet 163C, 246-258, doi:10.1002/ajmg.c.31381 (2013).

3 Mangold, E. et al. Sequencing the GRHL3 Coding Region Reveals Rare Truncating Mutations and a Common Susceptibility Variant for Nonsyndromic Cleft Palate. Am J Hum Genet 98, 755-762, doi:10.1016/j.ajhg.2016.02.013 (2016).

4 Garland, M. A., Reynolds, K. & Zhou, C. J. Environmental mechanisms of orofacial clefts. Birth Defects Res 112, 1660-1698, doi:10.1002/bdr2.1830 (2020).

5 Reynolds, K. et al. Genetics and signaling mechanisms of orofacial clefts. Birth Defects Res 112, 1588-1634, doi:10.1002/bdr2.1754 (2020).

6 Bush, J. O. & Jiang, R. Palatogenesis: morphogenetic and molecular mechanisms of secondary palate development. Development 139, 231-243, doi:10.1242/dev.067082 (2012).

7 Dixon, J. et al. Tcof1/Treacle is required for neural crest cell formation and proliferation deficiencies that cause craniofacial abnormalities. Proc Natl Acad Sci U S A 103, 13403-13408, doi:10.1073/pnas.0603730103 (2006).

8 Ji, Y. et al. Cellular and developmental basis of orofacial clefts. Birth Defects Res 112, 1558-1587, doi:10.1002/bdr2.1768 (2020).

9 Wang, Q. et al. Perturbed development of cranial neural crest cells in association with reduced sonic hedgehog signaling underlies the pathogenesis of retinoic-acid-induced cleft palate. Dis Model Mech 12, doi:10.1242/dmm.040279 (2019).

10 Humbert, J. et al. De Novo KAT5 Variants Cause a Syndrome with Recognizable Facial Dysmorphisms, Cerebellar Atrophy, Sleep Disturbance, and Epilepsy. Am J Hum Genet 107, 564-574, doi:10.1016/j.ajhg.2020.08.002 (2020).

11 Yang, J. et al. Integrating GWAS and eQTL to predict genes and pathways for non-syndromic cleft lip with or without palate. Oral Dis 27, 1747-1754, doi:10.1111/odi.13699 (2021).

12 Venkatesh, S. & Workman, J. L. Histone exchange, chromatin structure and the regulation of transcription. Nat Rev Mol Cell Biol 16, 178-189, doi:10.1038/nrm3941 (2015).

13 Hota, S. K. & Bruneau, B. G. ATP-dependent chromatin remodeling during mammalian development. Development 143, 2882-2897, doi:10.1242/dev.128892 (2016).

14 Li, Z. & Rasmussen, L. J. TIP60 in aging and neurodegeneration. Ageing Res Rev 64, 101195, doi:10.1016/j.arr.2020.101195 (2020).

15 Ishii, M. et al. A stable cranial neural crest cell line from mouse. Stem Cells Dev 21, 3069-3080, doi:10.1089/scd.2012.0155 (2012).

16 Cheng, J. et al. Merkel cell polyomavirus recruits MYCL to the EP400 complex to promote oncogenesis. PLoS Pathog 13, e1006668, doi:10.1371/journal.ppat.1006668 (2017).

17 Elsesser, O. et al. Chromatin remodeler Ep400 ensures oligodendrocyte survival and is required for myelination in the vertebrate central nervous system. Nucleic Acids Res 47, 6208-6224, doi:10.1093/nar/gkz376 (2019).

18 Pradhan, S. K. et al. EP400 Deposits H3.3 into Promoters and Enhancers during Gene Activation. Mol Cell 61, 27-38, doi:10.1016/j.molcel.2015.10.039 (2016).

19 Cordero, D. R. et al. Cranial neural crest cells on the move: their roles in craniofacial development. Am J Med Genet A 155A, 270-279, doi:10.1002/ajmg.a.33702 (2011).

20 Zhao, L. J., Loewenstein, P. M. & Green, M. Identification of a panel of MYC and Tip60 co-regulated genes functioning primarily in cell cycle and DNA replication. Genes Cancer 9, 101-113, doi:10.18632/genesandcancer.175 (2018).

21 Fröb, F. et al. Ep400 deficiency in Schwann cells causes persistent expression of early developmental regulators and peripheral neuropathy. Nat Commun 10, 2361, doi:10.1038/s41467-019-10287-w (2019).

22 Fujii, T., Ueda, T., Nagata, S. & Fukunaga, R. Essential role of p400/mDomino chromatin-remodeling ATPase in bone marrow hematopoiesis and cell-cycle progression. J Biol Chem 285, 30214-30223, doi:10.1074/jbc.M110.104513 (2010).

23 Wang, X. et al. Conditional depletion of the acetyltransferase Tip60 protects against the damaging effects of myocardial infarction. J Mol Cell Cardiol 163, 9-19, doi:10.1016/j.yjmcc.2021.09.012 (2022).

24 Wichmann, J. et al. Loss of TIP60 (KAT5) abolishes H2AZ lysine 7 acetylation and causes p53, INK4A, and ARF-independent cell cycle arrest. Cell Death Dis 13, 627, doi:10.1038/s41419-022-05055-6 (2022).

25 Bhattacharya, D., Azambuja, A. P. & Simoes-Costa, M. Metabolic Reprogramming Promotes Neural Crest Migration via Yap/Tead Signaling. Dev Cell 53, 199-211 e196, doi:10.1016/j.devcel.2020.03.005 (2020).

26 Nguyen, B. H., Ishii, M., Maxson, R. E. & Wang, J. Culturing and Manipulation of O9-1 Neural Crest Cells. J Vis Exp, 58346, doi:10.3791/58346 (2018).

27 Concordet, J. P. & Haeussler, M. CRISPOR: intuitive guide selection for CRISPR/Cas9 genome editing experiments and screens. Nucleic Acids Res 46, W242-W245, doi:10.1093/nar/gky354 (2018).

28 Cong, L. et al. Regulation of adiponectin and leptin secretion and expression by insulin through a PI3K-PDE3B dependent mechanism in rat primary adipocytes. Biochem J 403, 519-525 (2007).

29 Weider, M. et al. Elevated in vivo levels of a single transcription factor directly convert satellite glia into oligodendrocyte-like cells. PLoS Genet 11, e1005008, doi:10.1371/journal.pgen.1005008. PGENETICS-D-14-02490 [pii] (2015).

30 Love, M. I., Huber, W. & Anders, S. Moderated estimation of fold change and dispersion for RNA-seq data with DESeq2. Genome Biol 15, 550, doi:10.1186/s13059-014-0550-8 (2014).

31 Korotkevich, G. et al. Fast gene set enrichment analysis. bioRxiv doi.org/10.1101/060012 (2019).

32 Supek, F., Bosnjak, M., Skunca, N. & Smuc, T. REVIGO summarizes and visualizes long lists of gene ontology terms. PLoS One 6, e21800, doi:10.1371/journal.pone.0021800 (2011).

33 Ulgen, E., Ozisik, O. & Sezerman, O. U. pathfindR: An R Package for Comprehensive Identification of Enriched Pathways in Omics Data Through Active Subnetworks. Front Genet 10, 858, doi:10.3389/fgene.2019.00858 (2019).

34 Riccardi, C. & Nicoletti, I. Analysis of apoptosis by propidium iodide staining and flow cytometry. Nat Protoc 1, 1458-1461, doi:10.1038/nprot.2006.238 (2006).

35 Nagelreiter, F. et al. OPP Labeling Enables Total Protein Synthesis Quantification in CHO Production Cell Lines at the Single-Cell Level. Biotechnol J 13, e1700492, doi:10.1002/biot.201700492 (2018).

36 Schindelin, J. et al. Fiji: an open-source platform for biological-image analysis. Nat Methods 9, 676-682, doi:10.1038/nmeth.2019 (2012).

37 Petkau, N., Budak, H., Zhou, X., Oster, H. & Eichele, G. Acetylation of BMAL1 by TIP60 controls BRD4-P-TEFb recruitment to circadian promoters. Elife 8, doi:10.7554/eLife.43235 (2019).

38 Danielian, P. S., Muccino, D., Rowitch, D. H., Michael, S. K. & McMahon, A. P. Modification of gene activity in mouse embryos in utero by a tamoxifen-inducible form of Cre recombinase. Curr Biol 8, 1323-1326 (1998).

39 Srinivas, S. et al. Cre reporter strains produced by targeted insertion of EYFP and ECFP into the ROSA26 locus. BMC Dev Biol. 1, 4 (2001).

Acknowledgements

We thank Dirk Mielenz and Hans-Martin Jäck (Division of Immunology, Department of Medicine 3, FAU) for their help with Seahorse Measurements. R Fukunaga and G. Eichele are acknowledged for provision of Ep400 and Kat5 floxed mice. This work was supported by a grant from the IZKF Erlangen (E28).

Conflict of interests

The authors declare that there are no conflicts of interest.

Contributions

Ma.W., Mi.W. and L.G. conceived the study. S.G.-B. and T.S. performed and interpreted the experiment with help of Ma.W. S.G.-B., Mi.W. and L.G. wrote the manuscript.

Figure Legends

Figure 1: CRISPR/Cas9-dependent Kat5 inactivation in O9-1 cells. (a) Schematic representation of the *Kat5* gene with zoom-in on guide and adjacent sequences in the targeted exon 8 (red box). **(b)** Kat5 transcript levels in wildtype O9-1 cells (WT) and gene-edited clones Kat5/1 – Kat5/3 as determined by RT-PCR (n=3). Levels in wildtype cells were set to 1 ± SEM. **(c)** Kat5 protein levels in wildtype O9-1 cells (WT) and gene-edited clones as determined by Western blotting. Gapdh protein served as control. The size of detected proteins in kD (left) was estimated from co-electrophoresed marker proteins. **(d-f)** Summary of the consequences of Kat5 inactivation in O9-1 cells as determined by RNA-seq of gene-edited clones (n=3) and wildtype cells (n=4). Shown are the number of up-regulated (red) and down-regulated (blue) genes upon Kat5 inactivation (log2-fold ≥1, p-value ≤0.05) (d), a bi-clustering heatmap for visualization of the expression profile of the top 30 differentially expressed genes sorted and plotted by their (absolute) log2 transformed expression values in the samples (e), and a gene set enrichment analysis of DEGs to identify cellular processes and structures affected by Kat5 inactivation (f). Statistical significance was determined by one-way ANOVA and Dunnett's post test in b (***, P ≤0.001).

Figure 2: CRISPR/Cas9-dependent Ep400 inactivation in O9-1 cells. (a) Schematic representation of the *Ep400* gene with zoom-in on guide and adjacent sequences in the targeted exon 15 (red box). **(b)** Ep400 transcript levels in wildtype O9-1 cells (WT) and gene-edited clones Ep4005/1 – Ep4005/3 as determined by RT-PCR (n=3). Levels in wildtype cells were set to 1 ± SEM. **(c)** Immunocytochemical detection of Ep400 protein in wildtype O9-1 cells (WT) and gene-edited clones. DAPI was used to counterstain nuclei. Scale bar: 150µm. **(d-f)** Summary of the consequences of Ep400 inactivation in O9-1 cells as determined by RNA-seq of gene-edited clones (n=3) and wildtype cells (n=4). Shown are the number of up-regulated

(red) and down-regulated (blue) genes upon Ep400 inactivation (log2-fold ≥1, p-value ≤0.05) (d), a bi-clustering heatmap for visualization of the expression profile of the top 30 differentially expressed genes sorted and plotted by their (absolute) log2 transformed expression values in the samples (e), and a gene set enrichment analysis of DEGs to identify cellular processes and structures affected by Ep400 inactivation (f). Statistical significance was determined by one-way ANOVA and Dunnett's post test in b (**, P ≤0.01; ***, P ≤0.001).

Figure 3: Consequences of Kat5 and Ep400 inactivation in O9-1 cells. (a) KEGG pathway analysis for the identification of the main cellular processes (grey dots, red terms) and the key components (blue dots, black terms) affected by both Kat5 and Ep400 inactivation. **(b-e)** Comparison of O9-1 cells before (WT, black bars) and after inactivation of Kat5 (blue bars) or Ep400 (green bars) regarding rate of glycolytic ATP generation (determined in a Seahorse XFe analyzer as pmol per minute) (b), translation (determined as OPP incorporation in nascent transcripts with levels in WT cells set to 100%) (c), apoptosis (determined as percentage of cleaved caspase 3-positive cells among all cells) (d) and cell increase during 48h (determined by crystal violet staining with staining at 0 h set to 1) (e). Red line in (c) corresponds to OPP incorporation in the presence of cycloheximide. Values were averaged over all three clones and are expressed as mean ± SEM. **(f-i)** Percentage of cells undergoing mitosis (f,g) or being positive for phospho-histone H3 (pHH3) (h,i) in 30% confluent cultures as additional parameters for proliferation. Quantifications (f,h) and representative phase contrast images with overlaid fluorescent DAPI signal (violet–blue to white; scale bar: 100 µm; g) or immunofluorescent images (pHH3 in red, DAPI in blue; scale bar: 200 µm; i) are shown. Statistical significance was determined by one-way ANOVA and Dunnett's post test (ns, not significant; *, P ≤0.05; ***, P ≤0.001).

Figure 4: Developmental consequences of Kat5 and Ep400 inactivation in the cranial neural crest. (a) Schematic representation of the floxed alleles and the *Wnt1::Cre* used to inactivate *Kat5* and *Ep400* and the *Rosa26-stopflox-YFP* allele used to visualize successful inactivation in the cranial neural crest. Exons are depicted as black boxes, loxP sites as open triangles. pA, polyadenylation sequence; SA, adenovirus splice acceptor; PGK-Neo, pgk-neomycin; YFP, enhanced yellow fluorescent protein; Wnt1 prom, Wnt1 promoter; Cre, Cre recombinase; Wnt1 enh, Wnt1 enhancer. **(b-d)** Bright light (upper rows) and YFP-autofluorescent (lower rows) images of wholemount control (ctrl) embryos and age-matched heterozygous as well as homozygous embryos with Kat5 (Kat5Δ/+, Kat5Δ/Δ) and Ep400 (Ep400Δ/+, Ep400Δ/Δ) deletions at E9.5 (b), E10.5 (c) and E18.5 (d).

Figure 5: Consequences of Kat5 and Ep400 inactivation on proliferation and survival of the developing cranial neural crest. (a-c) Percentages of phosphohistone H3- (pHH3-) positive (a,b) and BrdU-labelled (c) neural crest cells in the first and second pharyngeal arches of control (ctrl) embryos and age-matched heterozygous as well as homozygous embryos (n=3 for each genotype) with Kat5 (Kat5Δ/+, checkered blue; Kat5Δ/Δ, blue) and Ep400 (Ep400Δ/+, checkered green; Ep400Δ/Δ, green) deletions at E9.5 (a) and E10.5 (b,c). Percentages are given as mean value ± SEM. **(d-e)** Rate of cleaved caspase 3-positive apoptotic cells in the various genotypes at E9.5 (d) and E10.5 (e). **(f)** Overall numbers of YFP-labelled cells in the second pharyngeal arches of the various genotypes at E10.5. Absolute numbers ± SEM correspond to cells per second branchial arch. **(g)** DAPI stain (upper rows) and YFP-autofluorescence (lower rows) of transverse sections from control, heterozygous and homozygous embryos with Kat5 or Ep400 deletions at E10.5 at the level of the second pharyngeal arch. Scale bar: 300 µm. Statistical significance was determined by one-way ANOVA and Sidak's post test (ns, not significant; *, $P \leq 0.05$; **, $P \leq 0.01$; ***, $P \leq 0.001$).

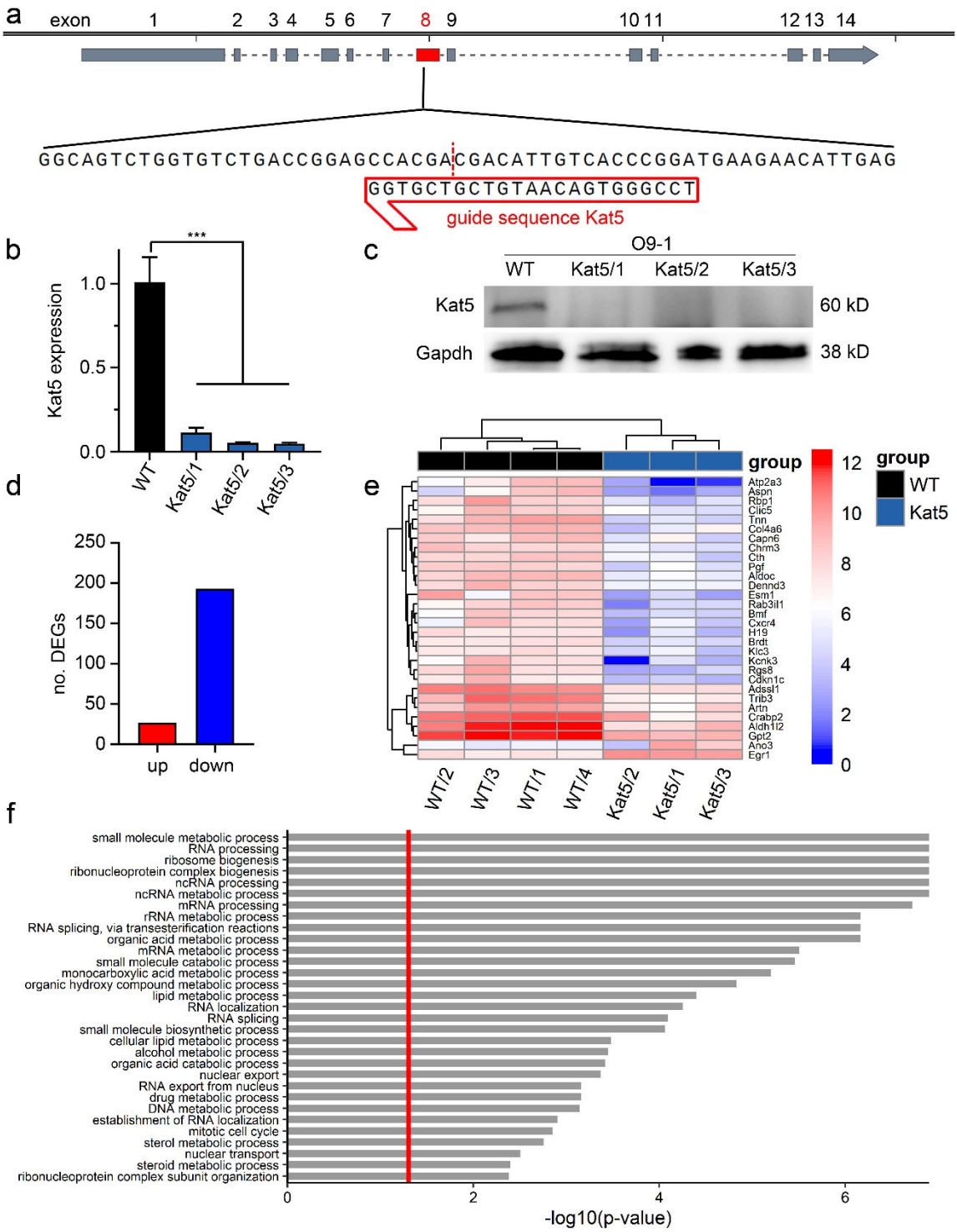
a
exon
1
2
3 4
5 6
7
8
9
10 11
12 13 14
GGCAGTCTGGTGTCTGACCGGAGCCACGACGACATTGTCACCCGGATGAAGAACATTGAG
GGTGCTGCTGTAACAGTGGGCCT
guide sequence Kat5
b
***
Kat5 expression
1.0
0.5
0.0
WT
Kat5/1
Kat5/2
Kat5/3
c
O9-1
WT
Kat5/1
Kat5/2
Kat5/3
Kat5
60 kD
Gapdh
38 kD
d
no. DEGs
250
200
150
100
50
0
up
down
e
group
12
10
8
6
4
2
0
group
WT
Kat5
Atp2a3
Aspn
Rbp1
Clic5
Tnn
Col4a6
Capn6
Chrm3
Cth
Pgf
Aldoc
Dennd3
Esm1
Rab3il1
Bmf
Cxcr4
H19
Brdt
Klc3
Konk3
Rgs8
Cdkn1c
Adssl1
Trib3
Artn
Crabp2
Aldh1l2
Gpt2
Ano3
Egr1
WT/2
WT/3
WT/1
WT/4
Kat5/2
Kat5/1
Kat5/3
f
small molecule metabolic process
RNA processing
ribosome biogenesis
ribonucleoprotein complex biogenesis
ncRNA processing
ncRNA metabolic process
mRNA processing
rRNA metabolic process
RNA splicing, via transesterification reactions
organic acid metabolic process
mRNA metabolic process
small molecule catabolic process
monocarboxylic acid metabolic process
organic hydroxy compound metabolic process
lipid metabolic process
RNA localization
RNA splicing
small molecule biosynthetic process
cellular lipid metabolic process
alcohol metabolic process
organic acid catabolic process
nuclear export
RNA export from nucleus
drug metabolic process
DNA metabolic process
establishment of RNA localization
mitotic cell cycle
sterol metabolic process
nuclear transport
steroid metabolic process
ribonucleoprotein complex subunit organization
0
2
4
6
-log10(p-value)

Figure 1

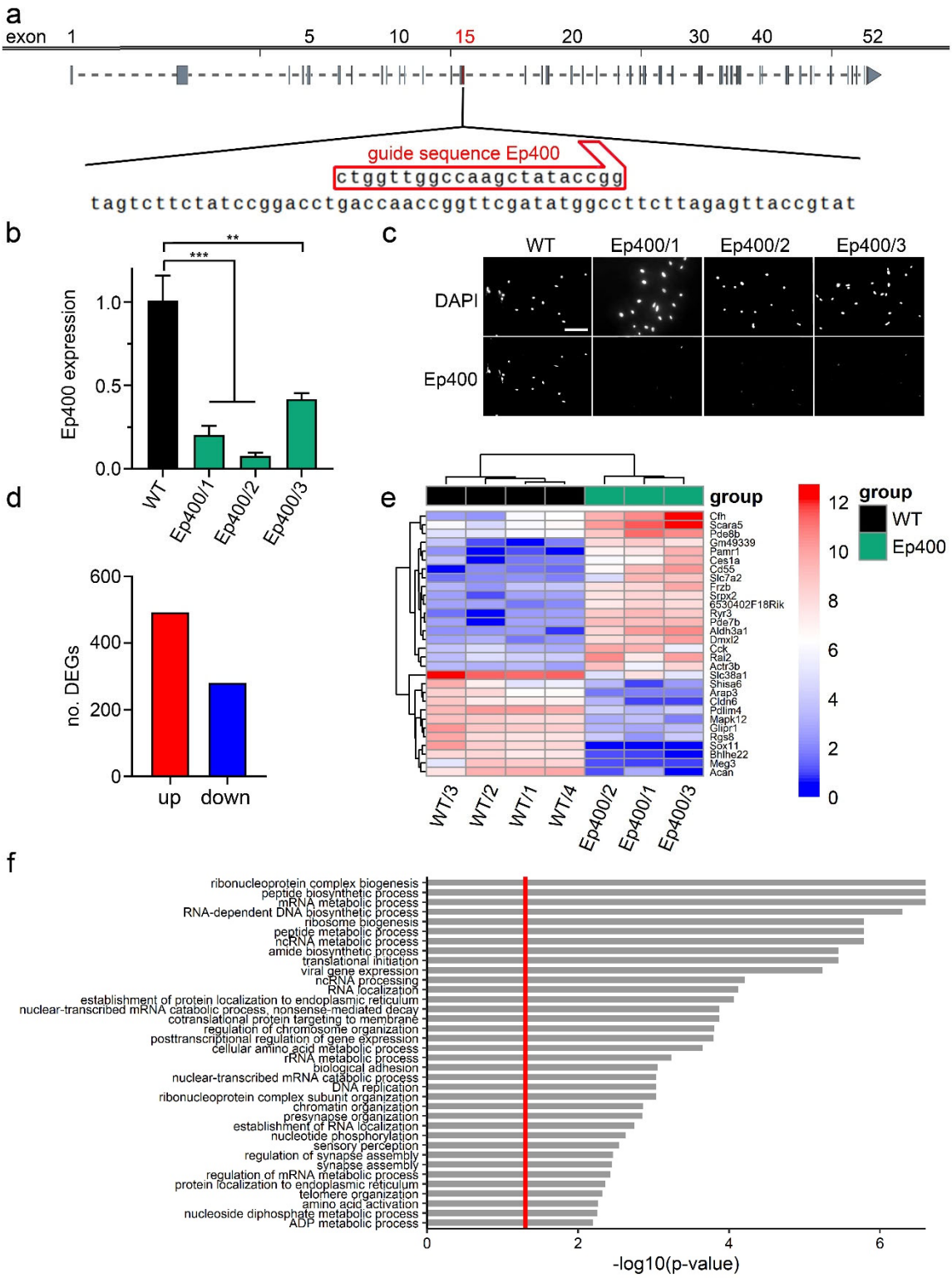
a
exon 1 5 10 15 20 30 40 52
guide sequence Ep400
ctggttggccaagctataccgg
tagtcttctatccggacctgaccaaccggttcgatatggccttcttagagttaccgtat
b
Ep400 expression
1.0
0.5
0.0
**
***
WT
Ep400/1
Ep400/2
Ep400/3
c
WT
Ep400/1
Ep400/2
Ep400/3
DAPI
Ep400
d
no. DEGs
600
400
200
0
up
down
e
group
WT
Ep400
Cfh
Scara5
Pde8b
Gm49339
Pamr1
Ces1a
Cd55
Slc7a2
Frzb
Srpx2
6530402F18Rik
Ryr3
Pde7b
Aldh3a1
Dmxl2
Cck
Ral2
Actr3b
Slc38a1
Shisa6
Arap3
Cldn6
Pdlim4
Mapk12
Gipr1
Rgs8
Sox11
Bhlhe22
Meg3
Acan
WT/3
WT/2
WT/1
WT/4
Ep400/2
Ep400/1
Ep400/3
12
10
8
6
4
2
0
f
ribonucleoprotein complex biogenesis
peptide biosynthetic process
mRNA metabolic process
RNA-dependent DNA biosynthetic process
ribosome biogenesis
peptide metabolic process
ncRNA metabolic process
amide biosynthetic process
translational initiation
viral gene expression
ncRNA processing
RNA localization
establishment of protein localization to endoplasmic reticulum
nuclear-transcribed mRNA catabolic process, nonsense-mediated decay
cotranslational protein targeting to membrane
regulation of chromosome organization
posttranscriptional regulation of gene expression
cellular amino acid metabolic process
rRNA metabolic process
biological adhesion
nuclear-transcribed mRNA catabolic process
DNA replication
ribonucleoprotein complex subunit organization
chromatin organization
presynapse organization
establishment of RNA localization
nucleotide phosphorylation
sensory perception
regulation of synapse assembly
synapse assembly
regulation of mRNA metabolic process
protein localization to endoplasmic reticulum
telomere organization
amino acid activation
nucleoside diphosphate metabolic process
ADP metabolic process
0
2
4
6
-log10(p-value)

Figure 2

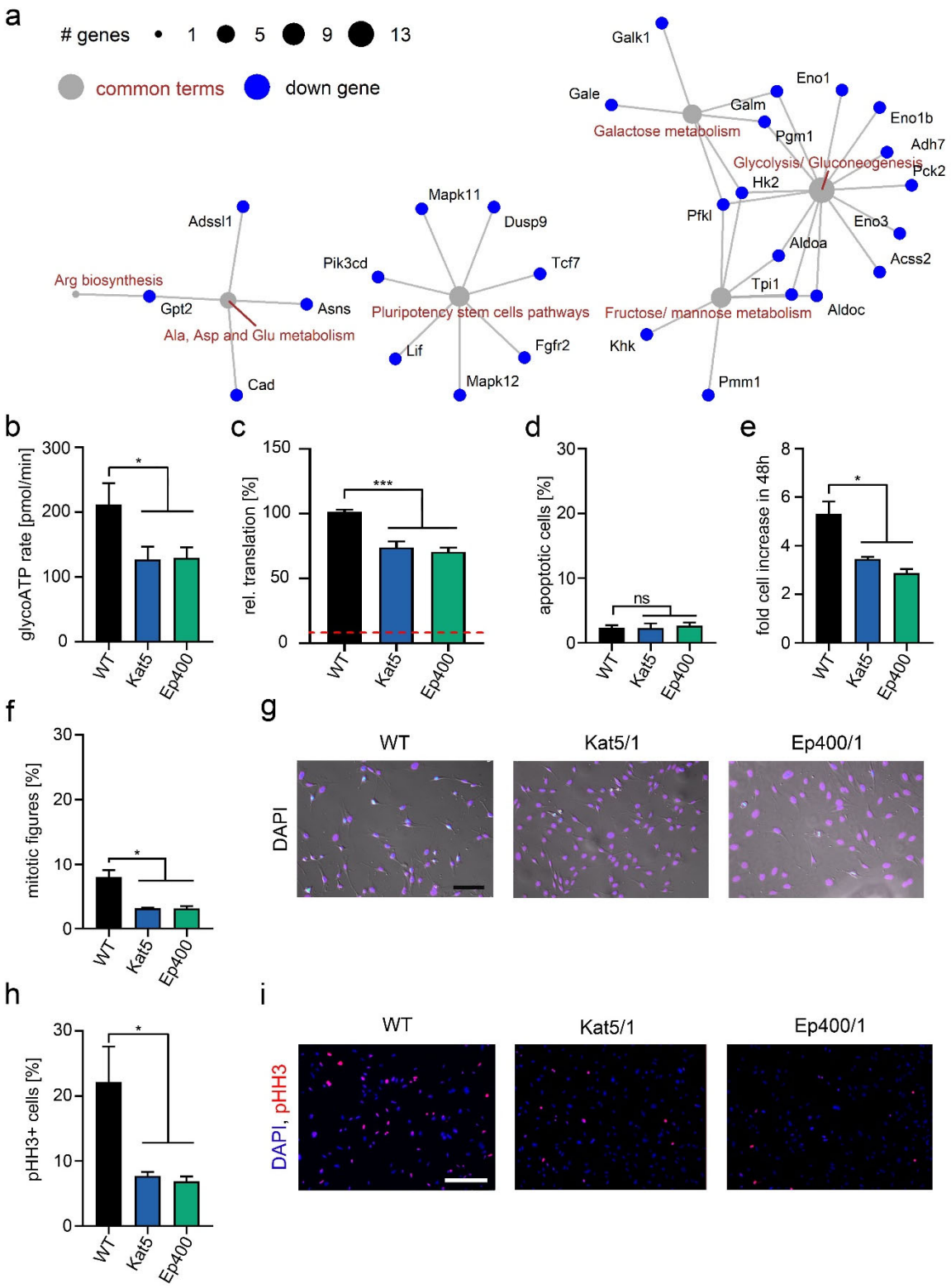
a
genes
1
5
9
13
common terms
down gene
Galk1
Gale
Galactose metabolism
Galm
Eno1
Eno1b
Pgm1
Adh7
Glycolysis/ Gluconeogenesis
Pck2
Hk2
Pfkl
Eno3
Aldoa
Acss2
Tpi1
Aldoc
Fructose/ mannose metabolism
Khk
Pmm1
Adssl1
Arg biosynthesis
Gpt2
Asns
Ala, Asp and Glu metabolism
Cad
Mapk11
Dusp9
Pik3cd
Tcf7
Pluripotency stem cells pathways
Lif
Fgfr2
Mapk12
b
glycoATP rate [pmol/min]
300
200
100
0
*
WT
Kat5
Ep400
c
rel. translation [%]
150
100
50
0
***
WT
Kat5
Ep400
d
apoptotic cells [%]
30
20
10
0
ns
WT
Kat5
Ep400
e
fold cell increase in 48h
8
6
4
2
0
*
WT
Kat5
Ep400
f
mitotic figures [%]
30
20
10
0
*
WT
Kat5
Ep400
g
WT
Kat5/1
Ep400/1
DAPI
h
pHH3+ cells [%]
30
20
10
0
*
WT
Kat5
Ep400
i
WT
Kat5/1
Ep400/1
DAPI, pHH3

Figure 3

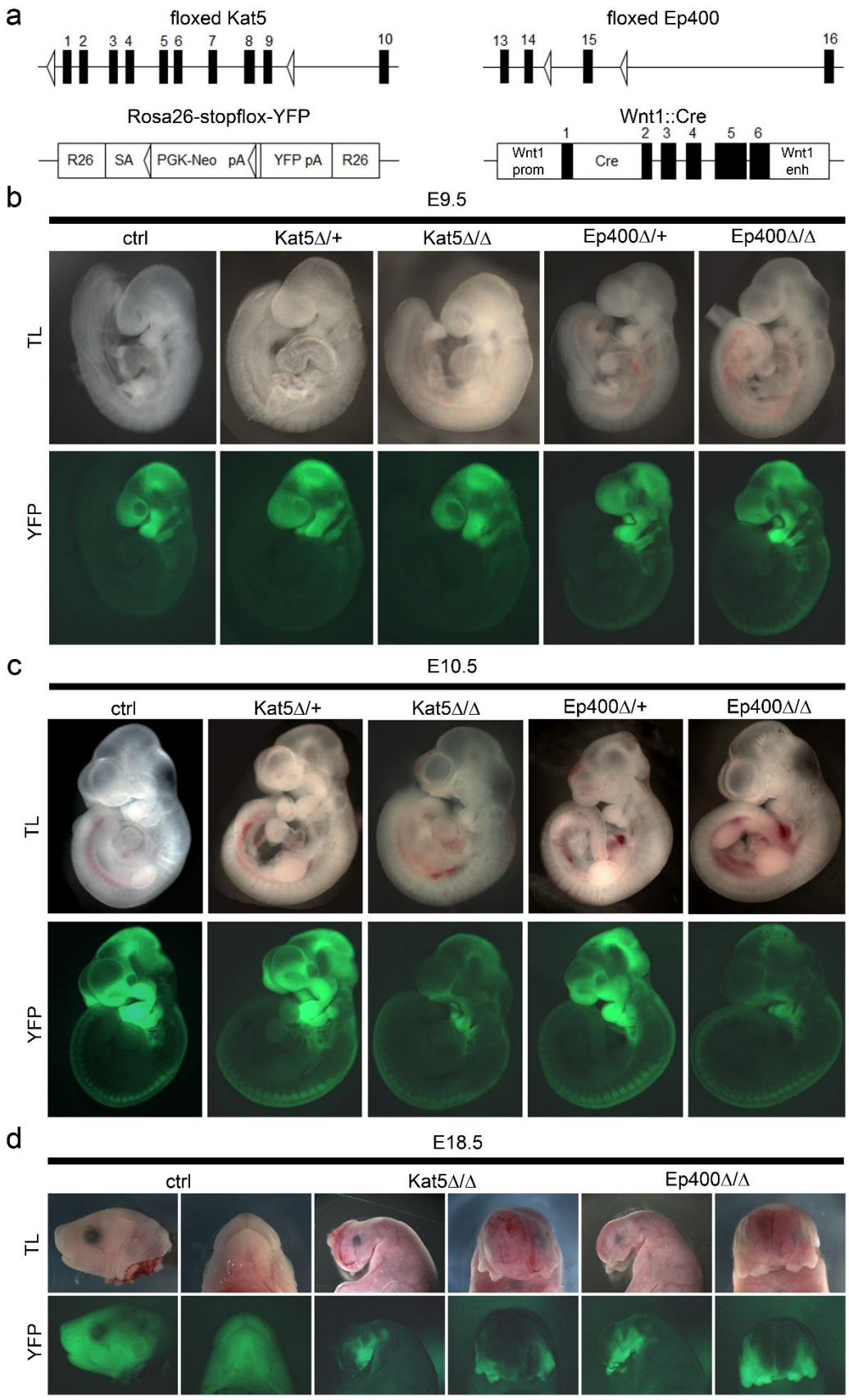
a
floxed Kat5
1 2 3 4 5 6 7 8 9 10
floxed Ep400
13 14 15 16
Rosa26-stopflox-YFP
R26 SA PGK-Neo pA YFP pA R26
Wnt1::Cre
1 2 3 4 5 6
Wnt1 prom
Cre
Wnt1 enh
b
E9.5
ctrl
Kat5Δ/+
Kat5Δ/Δ
Ep400Δ/+
Ep400Δ/Δ
TL
YFP
c
E10.5
ctrl
Kat5Δ/+
Kat5Δ/Δ
Ep400Δ/+
Ep400Δ/Δ
TL
YFP
d
E18.5
ctrl
Kat5Δ/Δ
Ep400Δ/Δ
TL
YFP

Figure 4

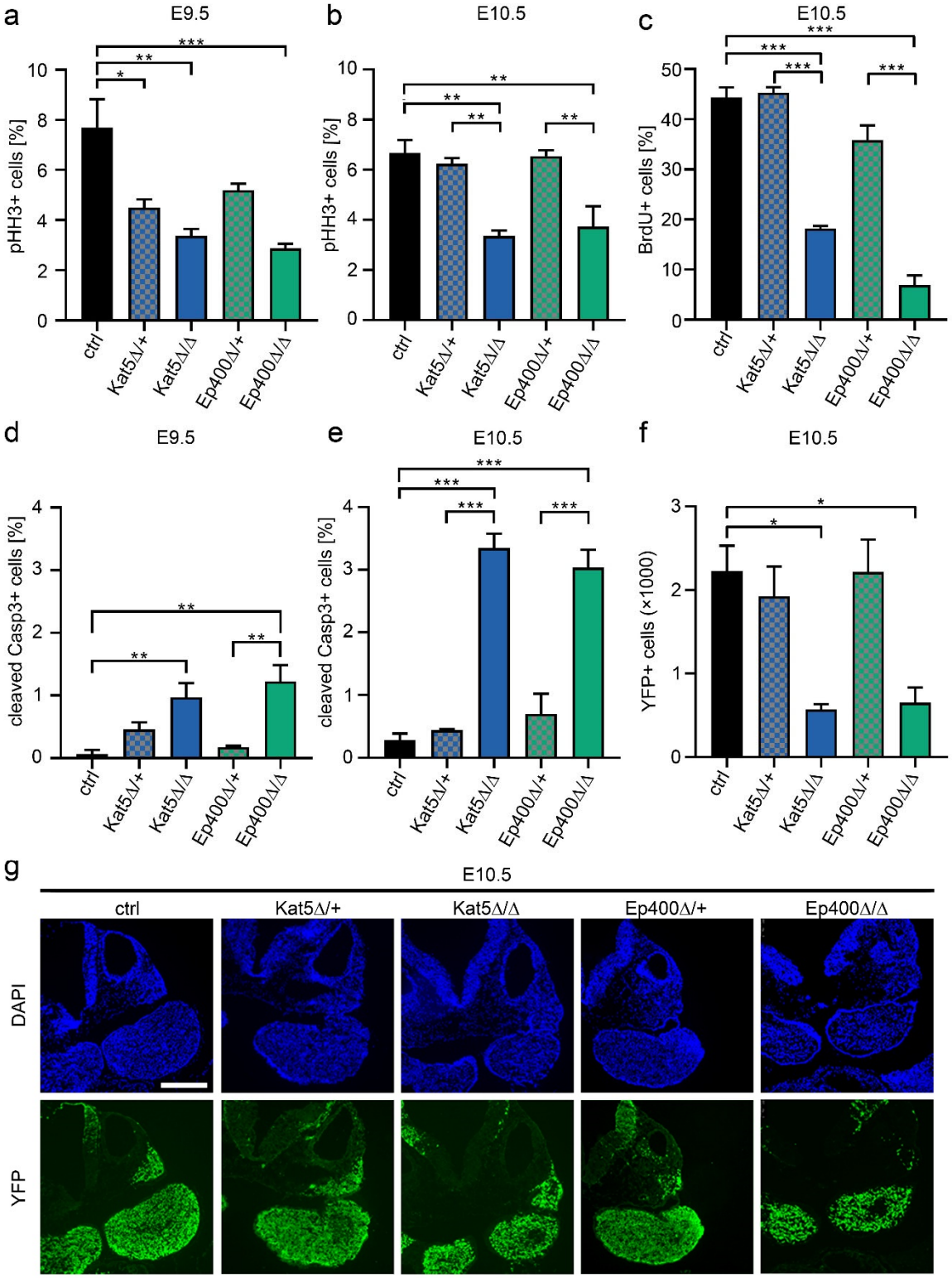
a
E9.5
pHH3+ cells [%]
b
E10.5
pHH3+ cells [%]
c
E10.5
BrdU+ cells [%]
d
E9.5
cleaved Casp3+ cells [%]
e
E10.5
cleaved Casp3+ cells [%]
f
E10.5
YFP+ cells (×1000)
ctrl
Kat5Δ/+
Kat5Δ/Δ
Ep400Δ/+
Ep400Δ/Δ
g
E10.5
DAPI
YFP

Figure 5